

# Nanometre-scale optical property fluctuations in $\text{Cu}_2\text{ZnSnS}_4$ revealed by low temperature cathodoluminescence

BG Mendis<sup>1</sup>, AA Taylor<sup>1,2\*</sup>, M Guennou<sup>3</sup>, DM Berg<sup>4\*\*</sup>, M Arasimowicz<sup>4</sup>, S Ahmed<sup>5</sup>, H Deligianni<sup>5</sup>, PJ Dale<sup>4</sup>

1. Dept. of Physics, Durham University, South Road, Durham, DH1 3LE, UK
2. EMPA, Laboratory for Mechanics and Nanostructures, Feuerwerkerstrasse 39, CH-3602 Thun, Switzerland.
3. Luxembourg Institute of Science and Technology, Materials Research and Technology Department, 41 rue du Brill, 4422 Belvaux, Luxembourg
4. Physics and Materials Science Research Unit, Université du Luxembourg, 41 rue du Brill, L-4422 Belvaux, Luxembourg
5. IBM, Thomas J. Watson Research Center, 1101 Kitchawan Road, Yorktown Heights, NY 10598, USA

\* Now at: Materials Department, University of California, Santa Barbara, CA 93106, USA.

\*\* Now at: Delaware State University, 1200 North DuPont Highway, Dover, DE 19901, USA.

## Abstract

Band tailing is a major contributing factor to the large open circuit voltage ( $V_{oc}$ ) deficit that is currently limiting  $\text{Cu}_2\text{ZnSnS}_4$  (CZTS) photovoltaic devices. It occurs in highly doped, highly compensated semiconductors and gives rise to a non-uniform electronic band structure. Here we report spatially resolved fluctuations in CZTS optical properties using low temperature cathodoluminescence (CL) in a scanning electron microscope (SEM). Principal component analysis reveals three CL peaks whose relative intensity vary across domains  $\sim 100$  nm in size. It is not known whether the non-uniform optical properties are due to changes in composition or due to structural order-disorder at constant composition. Measurement of composition with energy dispersive X-ray (EDX) analysis in an SEM and ordering with Micro-Raman mapping revealed CZTS to be uniform within the spatial resolution (estimated at  $\sim 0.4$   $\mu\text{m}$  and  $1.1$   $\mu\text{m}$  respectively) and sensitivity of the two techniques. The CL results are consistent with the presence of band tailing in CZTS.

## 1. Introduction

$\text{Cu}_2\text{ZnSnS}_4$  (CZTS) contains only earth abundant, non-toxic elements and is the leading absorber layer material for Tera Watt solar electricity generation [1]. The open circuit voltage ( $V_{oc}$ ) deficit is however large compared to the structurally similar  $\text{Cu}(\text{In,Ga})\text{Se}_2$  (CIGS) photovoltaic devices [2-3], and is the main reason for a relatively modest record cell efficiency of 12.6% for the S, Se variant  $\text{Cu}_2\text{ZnSn}(\text{S,Se})_4$  or CZTSSe [4]. A key difference between CZTS and CIGS is the extensive band tailing in the former [3,5]. Band tailing in CZTS is related to: (i) Urbach tails in absorption and quantum efficiency spectra [5], (ii) broadening of Raman vibration modes [6,7], (iii) S-shaped temperature dependence of the photoluminescence peak [8-9] and (iv) an anomalously long carrier lifetime at low temperature [3,10]. Band tailing

is common in highly doped, highly compensated semiconductors and is due to statistical fluctuations in the local dopant (i.e. donor and acceptor) concentration. This results in a spatially varying band structure with electron and hole potential wells [11], as illustrated in Figure 1. Electronic states are present within the band gap and the mobility of carriers within these tail states is smaller than ‘free’ (i.e. un-trapped) carriers. The lower overall mobility could therefore be a contributing factor to the short carrier diffusion length [2] and hence limited efficiency of CZTS.

Band tailing is due to band gap and/or electrostatic potential fluctuations. The former can be induced by ordering or, in the case of CZTSSe, variations in the anion and/or cation concentrations. On the other hand point defects in the form of vacancies and anti-site atoms can act as either donors or acceptors. Variations in dopant (i.e. donor and acceptor) concentration gives rise to electrostatic potential fluctuations. The low formation energy defects are typically anti-site atoms of Cu and Zn, such as the  $\text{Cu}_{\text{Zn}}$  acceptor or neutral  $[\text{Cu}_{\text{Zn}} + \text{Zn}_{\text{Cu}}]$  defect complex [12]. Neutron diffraction has revealed significant inter-mixing of Cu and Zn in the Wyckoff  $2c$  and  $2d$  positions of the kesterite phase (space group  $I\bar{4}$ ; [13]). Even for relatively slow sample cooling rates of 1 K/hr the Cu, Zn disorder can be as high as 30% [13]. Furthermore, chemical analysis in a scanning transmission electron microscope (STEM) has detected  $\text{Zn}_{\text{Cu}}$  donor clusters smaller than 5 nm in size [14], as well as  $\sim 20$  nm size domains where Cu substitutes for either Zn or Sn [15]. In the former case the local doping concentration, estimated at  $10^{22} \text{ cm}^{-3}$  [14], was high enough to render the semiconductor degenerate, while for the latter the amplitude of the composition fluctuation was estimated to be less than 1 at% or equivalently  $\sim 10^{20} \text{ cm}^{-3}$  [15].

The optical properties of CZTS have thus far largely been measured on the material as a whole, with less emphasis on uncovering any fluctuations within the material itself. Barragan *et al* [16] have reported a spatially non-uniform micro-Raman signal, but this was due to the presence of secondary phases such as ZnS, rather than an intrinsic property of the CZTS itself. In this paper we present evidence for spatially non-uniform optical properties in CZTS using cathodoluminescence (CL) in a scanning electron microscope (SEM). Photoluminescence spectra measured from bulk CZTS typically show a broad featureless peak [9], which makes it difficult to extract the underlying recombination pathways. The high spatial resolution in an SEM however provides more local information and by cooling the specimen close to liquid-He temperature the effect of phonon broadening of the luminescence peaks can also be reduced. It is shown that the optical properties of CZTS can fluctuate over domains  $\sim 100$  nm in size. The results complement previous findings on composition fluctuations in CZTS [14,15] and are consistent with the observation of band tailing in this material.

## 2. Experimental Methods

The sample precursor consisted of electrodeposited Cu/Sn/Zn layers [17] which were then sulphurised by annealing in a mixed S, SnS atmosphere [18] by placing 100 mg of S and 20 mg of SnS powder in a graphite box with an internal volume of  $20 \text{ cm}^3$ . The annealing procedure consisted of two steps: (i) a fast temperature ramp to  $100^\circ\text{C}$  at which the sample remained for 1 hr at pressures of less than 1 Pa of forming gas (10 %  $\text{H}_2$  in  $\text{N}_2$ ) and (ii) a fast temperature ramp to temperatures of around  $550^\circ\text{C}$  at which the sample was annealed for 2 hrs

in a 50 kPa atmosphere of forming gas. During the second annealing step the atmosphere inside the tube furnace further contained gaseous sulphur and tin-sulphide molecules at an undetermined partial pressure which originated from elemental sulphur and tin-sulphide pellets that were placed inside the furnace together with the samples at the beginning of the annealing procedure. After the second reaction step the samples were physically removed from the hot zone in order to quickly cool down the samples and abruptly stop any reaction.

Complete solar cell devices were made by chemically depositing a ~50 nm layer of CdS, followed by sputtering 80 nm of i-ZnO and 400 nm of Al:ZnO, and by e-beam evaporation of front contacts made from Ni then Al. Current density-voltage (JV) measurements on completed devices were made with a home built setup using a Keithly 2400 series source meter in a four wire kelvin probe configuration with 120 V ELH halogen lamp illumination calibrated with a certified mono crystalline silicon solar cell to give an output of 1000 Wm<sup>-2</sup> at 25°C. The kesterite devices were kept at 25°C using a peltier plate. The reference cell was certified under AM1.5 G illumination by the Fraunhofer ISE, Germany.

External quantum efficiency (EQE) measurements were made in a homemade system. White light passes through a Bentham TMC300 monochromator with 5 nm resolution to produce monochromatic light. The light is collimated and chopped with a Scitec instruments optical chopper with an output frequency of 133 Hz. The system is calibrated with Si and InGaAs photodiodes which were certified by the Physikalisch-Technische Bundesanstalt (German national standards laboratory). The photodiodes and kesterite cells were measured without bias using a homebuilt potentiostat acting as a current amplifier connected to an SR850 lock-in from Stanford Research Systems. The optical chopper outputs its frequency modulation to the lock-in for synchronization. Both JV and EQE measurements were made after annealing the devices on a hot plate with surface temperature of 200°C for 60 s in air.

For electron microscopy a ~2x1 mm area of the sample was ultrasonically cut and mechanically polished using a 0.1 µm grade diamond paper followed by low energy argon ion-polishing in a Gatan PIPS machine. This particular sample was not a completed device and had the front surface of the CZTS absorber layer exposed for electron microscopy analysis. A Hitachi SU-70 SEM at Durham was used for room temperature CL measurements of the ZnS secondary phases (section 3.2) as well as energy dispersive X-ray (EDX) analysis to determine the composition uniformity of CZTS. The operating voltage was 15 kV. A Tescan Lyra 3 dual-beam SEM at EMPA was used for EDX area mapping of the ZnS precipitates at 15 kV. Nano-indenters were placed on the sample surface to act as fiducial markers, so that approximately the same area could be used for analysis between different microscopes. Cross-section images were obtained using a 3 kV electron beam in an FEI Helios 600 focussed ion-beam (FIB) microscope at Durham. Prior to milling a platinum protective layer was deposited on the specimen surface in order to protect the underlying structure from ion-beam damage. Rough milling of the trench was carried out at 30 kV ion-beam voltage, while the cross-section was polished at 16 kV. The CL data on CZTS (section 3.3) was obtained using a prototype Attolight SEM operating at 5 kV beam voltage, with the sample liquid-Helium cooled to 10 K. Unfortunately the Attolight results preceded the other electron microscopy work in this paper and therefore it is unlikely the data was acquired from the same area of the sample. Nevertheless it should be noted that the overall microstructure did not vary between different regions of the sample. Attolight CL

data was processed using principal component analysis, implemented via the ‘Cornell Spectrum Imager’ freeware package [19].

Micro-Raman mapping was also performed on the same area of the sample, which was located by finding the nano-indentations under an optical microscope. A Renishaw inVia micro-Raman spectrometer was used for ZnS and CZTS mapping in two different configurations. For UV spectra, the 325 nm line of a He-Cd laser was used at ~0.8 mW power, focussed onto the sample with a microscope objective x40 with 0.5 numerical aperture (NA), in combination with a 2400 lines/mm grating, the spot size and spectral resolution being 0.8  $\mu\text{m}$  and 3.5  $\text{cm}^{-1}$  respectively. For the near-IR spectra, the excitation wavelength was 785 nm, laser power ~0.5 mW, the grating 1200 lines/mm, the microscope objective x100 with 0.9 NA, giving a spot size and spectral resolution of 1.1  $\mu\text{m}$  and 1.3  $\text{cm}^{-1}$  respectively. The maps were acquired over a 20x20  $\mu\text{m}^2$  square with 1  $\mu\text{m}$  step size. Principal component analysis was used to smooth the Raman spectra.

### 3. Results and Discussion

#### 3.1 Device electrical characterisation

The device parameters are non-ideal, such as a 14.9  $\text{mA}/\text{cm}^2$  short circuit current density, 564 mV open circuit voltage and 3.4% efficiency measured with a halogen lamp calibrated with a silicon reference cell to 1000  $\text{W}/\text{m}^2$ . Despite the poor performance the sample is nevertheless appropriate for investigating optical property fluctuations which is the main topic of this paper. This is because the EQE spectrum (Figure 2a) does not show a sharp onset at long wavelengths, indicating that the CZTS has significant band tails [5]. At energies close to the onset the absorption coefficient is approximately given by  $\log[1/(1-\text{EQE})]$  [3,5]; strictly speaking the internal quantum efficiency must be used instead of the EQE, although a comparison with optical reflection-transmission measurements shows that this approximation is still reasonable for the selenide variant,  $\text{Cu}_2\text{ZnSnSe}_4$  [5]. The EQE Tauc plot gave a room temperature band gap of  $1.63 \pm 0.03$  eV (Figure 2b). This is slightly larger than the 1.57 eV value measured using ellipsometry [20] and could be due to complications from band tailing, presence of ZnS [21] and voids (section 3.2) as well as the approximations discussed above. The absorption coefficient due to band tailing is typically modelled as an exponential decay below the band gap. However, a sharper decay of the form:

$$\alpha(E) = \alpha_0 \exp\left[-\left(\frac{E_g - E}{\sqrt{2}\gamma}\right)^2\right] \quad \dots (1)$$

where  $\alpha(E)$  is the absorption coefficient at energy  $E$ ,  $E_g$  is the band gap,  $\gamma$  the average potential well depth (Figure 1) and  $\alpha_0$  is a proportionality constant has also been proposed for heavily doped semiconductors [22]. This model gave a better fit to the EQE data (Figure 2c) with a  $\gamma$ -value of  $100.6 \pm 0.4$  meV. As expected the  $\gamma$ -value for our material is larger than that for the higher efficiency, hydrazine processed  $\text{Cu}_2\text{ZnSn}(\text{S},\text{Se})_4$  [3].

### 3.2 Microstructural characterisation

Figure 3a shows a backscattered SEM image of the CZTS absorber layer front surface. Nano-indenters are visible at the corners of the image and were used as fiducial markers for locating the region of interest (see section 2, Experimental Methods). Small precipitates of darker contrast, and hence lower average atomic number, are visible throughout the microstructure. A magnified view of the circled region in Figure 3a is shown in the figure inset and reveals the precipitates more clearly. EDX chemical maps for copper, zinc, tin and sulphur from approximately the same region are shown in Figures 3b-3e respectively. The precipitates are zinc-rich but depleted in copper and tin, while the sulphur concentration does not show any significant variation. This suggests that the precipitates are ZnS. Further evidence is obtained via room temperature panchromatic CL imaging where the precipitates are found to be highly luminescent (Figure 3f), consistent with previous observations for ZnS in CZTS [23]. Note that the coverage of ZnS precipitates appears to be higher in the CL image compared to the backscattered image and EDX chemical maps. This is because the resolution in a CL image is due to beam spreading as well as diffusion of the electron beam generated electron-hole pairs. A degradation in resolution is therefore observed if the carrier diffusion length is long compared to the beam interaction volume. Figure 3g is a FIB cross-section image of the specimen and shows that the ZnS precipitates are distributed throughout the absorber layer. Interfacial voids are also observed close to the back contact which would be a further contributing factor to the low device efficiency.

SEM-EDX was used to measure the composition uniformity of CZTS. Here particular attention must be paid to potential artefacts from ZnS secondary phases. Two separate regions which had fewer ZnS precipitates, as estimated qualitatively from the backscattered image, were chosen for chemical analysis. The dimensions of the two rectangular regions were  $5.7 \times 3.7 \mu\text{m}$  and  $8.5 \times 5.1 \mu\text{m}$  respectively. In each region the electron beam was scanned over a  $10 \times 10$  pixel raster to generate 100 EDX spectra for quantification. Figure 4a plots the cumulative distribution of  $\text{Cu}/(\text{Zn}+\text{Sn})$  atomic ratio values for the two regions and figure 4b is the equivalent plot for the  $\text{Zn}/\text{Sn}$  atomic ratio. The distribution for the two regions overlap for  $\text{Cu}/(\text{Zn}+\text{Sn})$  values greater than  $\sim 0.87$  and  $\text{Zn}/\text{Sn}$  values less than  $\sim 1.03$ . If the X-ray generation volume overlaps with any ZnS precipitates then this will cause a decrease in the overall measured  $\text{Cu}/(\text{Zn}+\text{Sn})$  ratio and a concomitant increase in  $\text{Zn}/\text{Sn}$  ratio, the level of variation being dependent on the amount of overlap. On the other hand compositions measured from only CZTS regions should show the same cumulative distribution profile independent of the area of analysis. From Figures 4a and 4b this suggests that for the CZTS in our sample the  $\text{Cu}/(\text{Zn}+\text{Sn})$  ratio varies between  $\sim 0.87$  and  $0.95$ , while the  $\text{Zn}/\text{Sn}$  ratio can take values between  $\sim 0.84$  and  $1.03$ . The CZTS phase itself is therefore Cu-poor and Zn-poor, although the sample overall is Zn-rich. The spread in  $\text{Cu}/(\text{Zn}+\text{Sn})$  and  $\text{Zn}/\text{Sn}$  ratios could suggest composition fluctuations within CZTS although the results must be treated with caution, since the absolute variation in Cu, Zn and Sn concentrations for the relevant spectra are no more than 2 at%, which is well within the accuracy of the measurement. In fact, previously reported composition fluctuations in CZTS were in the form of nanometre-sized domains [14-15]. Since this is considerably smaller than the X-ray generation volume for a 15 kV electron beam the effect of any composition fluctuations should be averaged out.

### 3.3 Micro-Raman mapping

Figure 5a shows the score image for the ZnS principal component obtained using the 325 nm laser. Higher ‘intensity’ corresponds to regions rich in ZnS (further details on principal component analysis is given in section 3.4). This is evident by comparing Raman spectra extracted from high and low intensity regions respectively. The former is characteristic of the resonant Raman spectrum for ZnS and consists of peaks for longitudinal optical (LO) and transverse optical (TO) phonons along with their overtones [24]. The feature at  $\sim 1598\text{ cm}^{-1}$  is assigned to the G peak of amorphous carbon, due to contamination present on the sample surface [25]. In fact the SEM-EDX maps (section 3.2) were acquired prior to Raman mapping, and some carbon contamination build up under the electron beam is inevitable. A typical Raman spectrum for CZTS under 785 nm near resonant laser excitation is shown in Figure 5b. The peaks at 287, 302, 336, 366 and  $373\text{ cm}^{-1}$  are known to be related to CZTS ordering [6, 25-26]. Specifically peak broadening is increased and the intensity ( $I$ ) ratios  $Q = I_{287}/I_{302}$ ,  $Q' = I_{336}/(I_{366} + I_{373})$  decrease on disordering [6,26], although no noticeable shift is observed in peak position [26]. Figures 5c and 5d show the spatial variation of position and width for the  $336\text{ cm}^{-1}$  peak along with a histogram showing the distribution of values. The mean and standard deviation of a Gaussian curve fitted to the histogram is also indicated in each figure. No significant variation in peak position and width is observed, indicating that the CZTS (dis)ordering is spatially uniform within the resolution limit of the technique. A more quantitative measure of ordering is obtained by analysing the  $Q'$  intensity ratio, as shown in Figure 5e.  $Q'$  can be as high as 5.7 for single crystals of CZTS grown by iodine vapour transport [27], while in the disordered state the value is less than unity [26-27]. A  $Q'$  value of 0.7 for our material indicates a high level of structural disorder, consistent with the broad EQE onset observed in Figure 2a.

### 3.4 Low temperature cathodoluminescence measurements

Figure 6 shows low temperature CL data acquired from the front surface of the CZTS absorber layer using the Attolight microscope (see section 2, Experimental Methods). The CL spectrum for each SEM beam scan position was stored as a ‘spectrum image’ [28]. Figure 6a is the secondary electron image and Figure 6b is the total (i.e. panchromatic) CL intensity plotted as a function of specimen position. Figure 6a has been rotated so that its orientation matches that of Figure 6b. A contaminant particle on the surface has been circled in both figures to act as a fiducial marker. The region of interest consists of several micrometre sized grains and grain boundaries. The CL emission is non-uniform with some grains appearing darker than others, while certain grain boundary segments, labelled ‘GB1’ and ‘GB2’ in Figure 6b, have higher intensity than the neighbouring grain interiors. A higher grain boundary intensity is unexpected, since these are typically regions of stronger non-radiative recombination [29]. However, Figure 6a also shows an increase in the secondary electron intensity in these same regions, which suggests that the anomaly could be a surface topography artefact, since the measured CL signal depends on the electron backscatter yield as well as total internal reflection. The CL spectrum summed from the entire spectrum image is shown in Figure 6c and reveals a broad featureless peak centred at  $\sim 917\text{ nm}$  (1.35 eV), similar to previous photoluminescence measurements (e.g. [8-9]).

The broadness of the luminescence peak, even at 10 K temperature, makes it difficult to analyse any variations in the spectra between different sample regions using the traditional method of Gaussian curve fitting. A multivariate statistical analysis method, principal component analysis (PCA) [30], is therefore used instead. In PCA each principal component represents a variation from the mean spectrum and is ranked in descending order of importance. The components are ‘orthogonal’ to one other, so that each component is a (mathematically) unique variation. For a data set that has not been centred (i.e. average set to zero) the first principal component is simply the average spectrum. The other principal component spectra represent deviations from the average spectrum and have a mean intensity of zero ([31]; negative intensity values are therefore permitted). Many of the lower ranked components are due to experimental noise in the data set, so that only the highest ranked components have physical meaning. The ‘dimensionality’ of the data set is therefore reduced, making interpretation easier. A further advantage is that PCA does not rely on any user input parameters or models (cf. Gaussian curve fitting), thereby enabling a more objective analysis. Further details of the application of PCA to spectrum images can be found in [31].

Figures 7a-7c show spectra for the second, third and fourth principal components from the data set in Figure 6 (the first principal component spectrum is the average spectrum, i.e. Figure 6c). The ‘scree plot’ is shown in Figure 7d. This plots the logarithm of the eigenvalue for each principal component and is essentially a measure of the significance of a given principal component. As discussed earlier the lower ranked components are due to noise and are represented by the linear portion of the scree plot [31]. A linear trend line, fitted to principal components above 20, is shown superimposed in Figure 7d. Principal components that deviate significantly from the straight line are likely to represent genuine physical variations. The fourth principal component is taken as the ‘cut off’ point, based on the deviation of the principal component value from the linear trend line and appearance of the component maps (see below; principal components due to noise in the raw data set tend to produce component maps that are noisy and featureless).

Figures 8a-8c show the component maps for the second, third and fourth principal components respectively. A component map plots the weighting of a given principal component as a function of specimen position. Bright regions in a given component map have local spectra that tend to deviate from the average spectrum in a manner indicative of the relevant principal component (note that other principal components may also have non-zero weighting in the same region). Figures 8a-8c reveal bright regions ~100 nm in size. Furthermore the second principal component (PC2) has a lower weighting at the grain boundaries (Figure 8a), although no difference between grain boundaries and grain interiors is observed for PC3 and PC4. CL spectra were extracted from the brightest region (circled) from each component map and plotted in Figure 8d; their relation to the principal component, and hence deviation from the mean, is apparent by comparing with Figures 7a-7c respectively. Spectra extracted from other bright regions in the component maps showed similar features to those in Figure 8d. The spectra are a combination of three broad peaks labelled P1, P2 and P3. The PC2 spectrum has a higher intensity of P2, PC3 consists mainly of P2 and P3, while PC4 is comprised mainly of P1 and P3. Two Gaussian curves were fitted to the PC4 spectrum and from this the peak positions for P1 and P3 were estimated to be 876 nm (1.42 eV) and 930 nm (1.33 eV) respectively. PC4 is likely to contain some intensity from P2 as well, so that the P1 and P3

peak positions, expressed as wavelength, will be somewhat over- and under-estimated respectively. Peak positions must therefore be treated with caution. The P2 peak position was estimated to be 907 nm (1.37 eV) by fitting a single Gaussian to the PC2 spectrum.

The bright regions in Figures 8a-8c could potentially be an artefact from interference effects [32] which occurs when the CZTS absorber layer acts as a Fabry-Perot etalon, as shown in Figure 9. Light emitted toward the back contact can undergo multiple reflections before escaping the CZTS layer. The extra path length causes a phase shift, so that constructive or destructive interference is possible depending on the conditions. If the etalon thickness varies, for example due to an uneven CZTS front surface or back contact, then spurious maxima may be present in the CL spectrum, which could be mistaken for genuine peaks. However, the ~100 nm size of the bright regions is too small to be treated as a separate etalon of unique thickness. Consider an emission event that takes place in the middle of the CZTS absorber layer. For interference to occur at least two reflections off the back contact is required. From Figure 9 the minimum lateral size of the etalon is therefore  $(3.5t)\tan\theta$ , where  $t$  is the CZTS layer thickness (i.e. ~1  $\mu\text{m}$ , as measured from Figure 3g). Equating this to 100 nm gives a maximum emission angle  $\theta$  of only  $2^\circ$ . Luminescence from electron-hole pair recombination is isotropic, so that  $\theta$  corresponds to a solid angle of  $5 \times 10^{-3}$  steradian. However in practice only emission angles up to the critical angle for total internal reflection at the CZTS-air boundary are detected. The critical angle is determined by the refractive index ( $n$ ) of CZTS and Snell's law. Substituting  $n = 2.8$  ([1]; valid for the peak wavelength in Figure 6c) gives a critical angle of  $21^\circ$  or a collection solid angle of 0.83 steradian (note that emission towards the front surface and back contact must both be taken into account). The light undergoing interference within the etalon boundaries is therefore less than 1% of the total emission detected. This is sufficiently small to ignore any interference effects. To increase the fraction to a more reasonable 10%  $\theta$  will have to be  $6.6^\circ$  or equivalently  $t$  must be 247 nm. The large voids at the back contact interface in the FIB cross-section image (Figure 3g) have lateral dimensions significantly greater than 100 nm and do not reduce the absorber layer thickness to the desired value. Furthermore any roughness of the CZTS front surface is minimised by polishing the sample and would nevertheless have been apparent in the secondary electron image (Figure 6a) as an enhanced intensity from the side walls of the asperity [33].

Having ruled out interference as an artefact it is important to identify the nature of the CL peaks in Figure 8d. Photoluminescence has also uncovered three luminescence peaks in CZTS by varying the measurement temperature [34-35]. Our results indicate three peaks at the same temperature, albeit in varying amounts in different specimen regions. The radiative transitions in a highly doped semiconductor are indicated in Figure 1. These can be classified as interband (i.e. band to band BB, band to tail BT and tail to tail TT) and impurity related transitions (i.e. band to impurity BI and tail to impurity TI) [11]. Here 'band' in BB, BT etc represents untrapped electronic states with maximum carrier mobility (Figure 1), while 'impurity' is the acceptor in  $p$ -type CZTS. In previous studies [34-35] the three peaks have been labelled as BB, BT and BI, although, apart from perhaps the BB peak, there is no unambiguous evidence for such an identification. For a BB transition the peak energy is at  $(E_g + \frac{1}{2}kT)$  [36], i.e. close to the band gap energy  $E_g$  at low temperatures. In Figure 8d the highest energy peak P1 is at 1.42 eV, significantly below the band gap of 1.63 eV, and cannot therefore be a BB transition. P1 could however be a TT transition, based on a measured tail energy of 101 meV. There is

nevertheless some doubt whether this value is applicable to low temperature CL, since it was extracted from room temperature EQE measurements. Potential wells with depth less than  $kT$  should have a minor effect on the EQE, since these can be overcome by thermal excitation. The average tail energy  $\gamma$ , extracted from the room temperature EQE data, is therefore biased towards the deeper (i.e.  $>25$  meV) potential wells. On the other hand for low temperature CL, assuming low injection conditions, the excess carriers generated by the electron beam thermalise to the local potential well minimum. The room temperature EQE tail energy may therefore be an overestimate for low temperature CL.

Assuming P1 is a TT transition then P2 and P3 could be BI and TI transitions respectively. However, the energy separation between P2 and P3 is only  $\sim 34$  meV, considerably smaller than the 101 meV average tail energy. The discrepancy is too large to be due to the uncertainty in CL peak positions. Grossberg *et al* [34, 35] have labelled two of their photoluminescence peaks, measured from bulk samples, as BI transitions that arise from the same acceptor impurity, but two different band gap values depending on the CZTS being ordered or disordered with respect to Cu and Zn. A band gap energy increase of 110 meV has been observed experimentally [7] on ordering and is supported by theoretical calculations which show that the  $[\text{Cu}_{\text{Zn}} + \text{Zn}_{\text{Cu}}]$  defect complex can lower the band gap [38-40]. The P2 peak could therefore potentially be due to ordering, although with no supporting evidence the exact nature of the transitions remains unresolved. The peaks are nevertheless unlikely to be due to ZnS secondary phases. The wider band gap of ZnS means that emission is typically at much shorter wavelengths [41] and examination of the full CL spectrum, which extends up to 638 nm (i.e. 1.94 eV), did not reveal any additional intensity. Furthermore from Figure 3f the average diameter of the ZnS precipitates is measured to be  $2.0 \pm 0.3$   $\mu\text{m}$ , which is significantly larger than the  $\sim 100$  nm domains extracted from PCA.

It is interesting that fluctuations in the optical properties of CZTS were detected using CL, but EDX did not detect any composition variations larger than the accuracy of the method (section 3.2). The experimental conditions and sensitivity of the two methods are however not the same. For example EDX measurements were carried out at 15 kV, while the beam voltage for CL was only 5 kV. The degree of beam spreading for EDX is not favourable for detecting the  $\sim 100$  nm size domains in Figures 8a-8c. From Monte Carlo simulations [42] of the beam spreading it is estimated that at 15 kV the spatial resolution of the EDX maps is  $\sim 0.4$   $\mu\text{m}$ . The analytical volume for CL could in principle be smaller due to the lower beam voltage, although carrier diffusion also needs to be taken into account. Even if the fluctuations were of the right size for EDX the change in composition must be larger than the sensitivity of the measurement, which is typically a few atom percent. However, 1 at% corresponds to a doping concentration of  $\sim 10^{20}$   $\text{cm}^{-3}$  in CZTS, well above the doping levels for a photovoltaic absorber layer. On the other hand the sensitivity of CL to point defects and doping is well documented. Furthermore the CL signal will depend on the structural ordering as well as chemistry of the material, while SEM-EDX largely depends on the latter. For example anti-site atoms and/or vacancies may be present while still preserving the overall composition (e.g. the  $[\text{Cu}_{\text{Zn}} + \text{Zn}_{\text{Cu}}]$  defect complex). This could alter the CL signal by creating additional radiative recombination channels, by changing the local band gap or by quenching the intensity via non-radiative recombination. On the other hand EDX will not detect any change due to the uniform composition. Micro-Raman mapping did not detect any variation in ordering, but here the spot size of the laser was 1.1  $\mu\text{m}$ ,

significantly larger than the ~100 nm domain sizes observed in CL. A comparison of the ZnS maps in Figures 3c and 5a suggests that the resolution for Raman may be less than even the SEM-EDX conditions used here.

Finally consider the lower weighting of the second principal component (PC2) at the grain boundaries (Figure 8a). Romero *et al* [43] have reported a red shift in the CL peak at CIGS grain boundaries, which was also present, but less obvious, in CZTS. PC2 mainly consists of the P2 peak at 907 nm (Figure 8d) which is slightly blue shifted with respect to the average spectrum centred at 917 nm (Figure 6c). Our results are therefore consistent with the findings of Romero *et al* [43]. However, PCA analysis on other regions of the specimen showed that the lower PC2 weighting at grain boundaries was not as well defined. As an example Figures 10a and 10b show the secondary electron and panchromatic CL images for a different specimen region. Figure 10a has been rotated so that its orientation matches that of Figure 10b and a contaminant particle has been circled in both images to act as a fiducial marker. The second principal component spectrum is shown in Figure 10c, along with its component map in Figure 10d. The principal component in Figure 10c is similar to that in Figure 7a indicating that they are both due to the same physical variation. Bright regions are observed within the grain interiors in the component map (an example is circled in Figure 10d) indicating non-uniform optical properties, although the weighting of the principal component does not vary significantly at the grain boundaries (note that the intensity range of Figures 8a and 10d are similar). The recombination mechanisms are likely to depend on the grain boundary character and therefore some variation between grain boundaries is expected.

#### **4. Conclusions**

The optical properties of CZTS has been investigated at high spatial resolution using low temperature CL. Principal component analysis of the data has revealed three CL peaks at 876, 907 and 930 nm wavelength whose origin is not well understood. The relative intensities of these three peaks vary with specimen position, in some cases forming domains ~100 nm in size. This indicates fluctuations in the optical properties of CZTS, similar to composition fluctuations that have been reported previously. Optical properties can vary due to changes in composition as well as structural order-disorder at constant composition. SEM-EDX and micro-Raman mapping did not detect a statistically significant change in the CZTS composition and ordering respectively, although it should be noted that the measurement sensitivity (for EDX)/ resolution (for Raman) are not optimised. EQE measurements for the completed device showed significant band tailing, with an average potential well depth of 101 meV. The optical property fluctuations observed in CL are consistent with band tailing. Finally a lower weighting of the 907 nm CL peak is observed at the grain boundaries, although this depends on the grain boundary character.

#### **5. Acknowledgements**

Durham and Luxembourg co-authors would like to thank EPSRC (EP/K001620/1) and FNR Luxembourg (ATTRACT) for funding respectively. Principal component analysis on low temperature cathodoluminescence data was carried out using the Cornell Spectrum Imager

freeware [19]. The underlying research data for this paper is available in accordance with EPSRC open data policy from doi:10.15128/r147429912z.

## References

- [1] K Ito, *Copper Zinc Tin Sulfide-Based Thin Film Solar Cells*, Wiley (2015).
- [2] O Gunawan, TK Todorov and DB Mitzi, Loss mechanisms in hydrazine-processed  $\text{Cu}_2\text{ZnSn}(\text{Se},\text{S})_4$  solar cells, *Appl. Phys. Lett.* **97** (2010) 233506 (3 pages).
- [3] T Gokmen, O Gunawan, TK Todorov and DB Mitzi, Band tailing and efficiency limitation in kesterite solar cells, *Appl. Phys. Lett.* **103** (2013) 103506 (5 pages).
- [4] MA Green, K Emery, Y Hishikawa, W Warta and ED Dunlop, Solar cell efficiency tables (version 49), *Prog. Photovolt: Res. Appl.* **25** (2017) 3-13.
- [5] S Siebentritt, G Rey, A Finger, D Regesch, J Sendler, TP Weiss and T Bertram, What is the bandgap of kesterite?, *Sol. Energy Mater. Sol. Cells* **158** (2016) 126-129.
- [6] JJS Scragg, L Choubrac, A Lafond, T Ericson and C Platzer-Björkman, A low-temperature order-disorder transition in  $\text{Cu}_2\text{ZnSnS}_4$  thin films, *Appl. Phys. Lett.* **104** (2014) 041911 (4 pages).
- [7] G Rey, A Redinger, J Sendler, TP Weiss, M Thevenin, M Guennou, BE Adib and S Siebentritt, The band gap of  $\text{Cu}_2\text{ZnSnSe}_4$ : Effect of order-disorder, *Appl. Phys. Lett.* **105** (2014) 112106 (4 pages).
- [8] JP Teixeira, RA Sousa, MG Sousa, AF da Cunha, PA Fernandes, PMP Salomé and JP Leitão, Radiative transitions in highly doped and compensated chalcopyrites and kesterites: The case of  $\text{Cu}_2\text{ZnSnS}_4$ , *Phys. Rev. B* **90** (2014) 235202 (10 pages).
- [9] DP Halliday, R Claridge, MCJ Goodman, BG Mendis, K Durose and JD Major, Luminescence of  $\text{Cu}_2\text{ZnSnS}_4$  polycrystals described by the fluctuating potential model, *J. Appl. Phys.* **113** (2013) 223503 (10 pages).
- [10] LQ Phuong, M Okano, Y Yamada, A Nagaoka, K Yoshino and Y Kanemitsu, Temperature-dependent photocarrier recombination dynamics in  $\text{Cu}_2\text{ZnSnS}_4$  single crystals, *Appl. Phys. Lett.* **104** (2014) 081907 (4 pages).
- [11] AP Levanyuk and VV Osipov, Edge luminescence of direct-gap semiconductors, *Usp. Fiz. Nauk.* **133** (1981) 427.
- [12] S Chen, J-H Yang, XG Gong, A Walsh and S-H Wei, Intrinsic point defects and complexes in the quaternary kesterite semiconductor  $\text{Cu}_2\text{ZnSnS}_4$ , *Phys. Rev. B* **81** (2010) 245204 (10 pages).
- [13] S Schorr, H-J Hoebler and M Tovar, A neutron diffraction study of the stannite-kesterite solid solution series, *Eur. J. Mineral.* **19** (2007) 65-73.
- [14] BG Mendis, MD Shannon, MCJ Goodman, JD Major, R Claridge, DP Halliday and K Durose, Direct observation of Cu, Zn cation disorder in  $\text{Cu}_2\text{ZnSnS}_4$  solar cell absorber material using aberration corrected scanning transmission electron microscopy, *Prog. Photovolt: Res. Appl.* **22** (2014) 24-34.
- [15] JA Aguiar, ME Erkan, DS Pruzan, A Nagaoka, K Yoshino, H Moutinho, M Al-Jassim and MA Scarpulla, Cation ratio fluctuations in  $\text{Cu}_2\text{ZnSnS}_4$  at the 20 nm length scale investigated by analytical electron microscopy, *Phys. Status Solidi A* **213** (2016) 2392-2399.
- [16] AA Barragan, H Malekpour, S Exarhos, AA Balandin and L Mangolini, Grain-to-Grain Compositional Variations and Phase Segregation in Copper-Zinc-Tin-Sulfide Films, *Appl. Mater. Interfaces* **8** (2016) 22971-22976.

- [17] S Ahmed, KB Reuter, O Gunawan, L Guo, LT Romankiw and H Deligianni, A High Efficiency Electrodeposited  $\text{Cu}_2\text{ZnSnS}_4$  Solar Cell, *Adv. Energy Mat.* **2** (2012) 253-259.
- [18] DM Berg, A Crossay, J Guillot, V I-Roca, A P-Rodriguez, S Ahmed, H Deligianni, S Siebentritt and PJ Dale, Simplified formation process for  $\text{Cu}_2\text{ZnSnS}_4$ -based solar cells, *Thin Solid Films* **573** (2014) 148-158.
- [19] P Cueva, R Hovden, JA Mundy, HL Xin and DA Muller, Data Processing for Atomic Resolution Electron Energy Loss Spectroscopy, *Microsc. Microanal.* **18** (2012) 667-675.
- [20] S-Y Li, C Hägglund, Y Ren, JJS Scragg, JK Larsen, C Frisk, K Rudisch, S Englund and C Platzer-Björkman, Optical properties of reactively sputtered  $\text{Cu}_2\text{ZnSnS}_4$  solar absorbers determined by spectroscopic ellipsometry and spectrophotometry, *Sol. Energy Mater. Sol. Cells* **149** (2016) 170-178.
- [21] S Ahn, S Jung, J Gwak, A Cho, K Shin, K Yoon, D Park, H Cheong and JH Yun, Determination of band gap energy ( $E_g$ ) of  $\text{Cu}_2\text{ZnSnSe}_4$  thin films: On the discrepancies of reported band gap values, *Appl. Phys. Lett.* **97** (2010) 021905 (3 pages).
- [22] JK Katahara and HW Hillhouse, Quasi-Fermi level splitting and sub-bandgap absorptivity from semiconductor photoluminescence, *J. Appl. Phys.* **116** (2014) 173504 (12 pages).
- [23] BG Mendis, MCJ Goodman, JD Major, AA Taylor, K Durose and DP Halliday, The role of secondary phase precipitation on grain boundary electrical activity in  $\text{Cu}_2\text{ZnSnS}_4$  (CZTS) photovoltaic absorber layer material, *J. Appl. Phys.* **112** (2012) 124508 (10 pages).
- [24] JF Scott, TC Damen, WT Silfvast, RCC Leite and LE Cheesman, Resonant Raman scattering in ZnS and ZnSe with the cadmium laser, *Opt. Commun.* **1** (1970) 397-399.
- [25] AC Ferrari and J Robertson, Resonant Raman spectroscopy of disordered, amorphous and diamond-like carbon, *Phys. Rev. B* **64** (2001) 075414.
- [26] M Paris, L Choubrac, A Lafond, C Guillot-Deudon, S Jobic, Solid-State NMR and Raman Spectroscopy To Address the Local Structure of Defects and the Tricky Issue of the Cu/Zn Disorder in Cu-Poor, Zn-Rich CZTS Materials, *Inorg. Chem.* **53** (2014) 8646-8653.
- [27] TM Ng, MT Weller, GP Kissling, LM Peter, P Dale, F Babbe, J de Wild, B Wenger, HJ Snaith and D Lane, Optoelectronic and spectroscopic characterization of vapour-transport grown  $\text{Cu}_2\text{ZnSnS}_4$  single crystals, *J. Mat. Chem. A* **5** (2017) 1192-1200.
- [28] C Jeanguillaume and C Colliex, Spectrum Image – the next step in EELS digital acquisition and processing, *Ultramicroscopy* **28** (1989) 252-257.
- [29] BG Mendis, D Gachet, JD Major and K Durose, Long Lifetime Hole Traps at Grain Boundaries in CdTe Thin-Film Photovoltaics, *Phys. Rev. Lett.* **115** (2015) 218701 (5 pages).
- [30] IT Jolliffe, *Principal Component Analysis*, 2<sup>nd</sup> Edition, Springer-Verlag, New York (2002).
- [31] M Bosman, M Watanabe, DTL Alexander and VJ Keast, Mapping chemical and bonding information using multivariate analysis of electron energy-loss spectrum images, *Ultramicroscopy* **106**, (2006) 1024-1032.
- [32] R Djemour, A Redinger, M Mousel, L Gütay and S Siebentritt, Multiple phases of  $\text{Cu}_2\text{ZnSnSe}_4$  detected by room temperature photoluminescence (vol 116, 073509, 2014), *J. Appl. Phys.* **118** (2015) 089902 (3 pages).
- [33] JI Goldstein, DE Newbury, DC Joy, CE Lyman, P Echlin, E Lifshin, L Sawyer and JR Michael, *Scanning Electron Microscopy and X-ray Microanalysis*, 3<sup>rd</sup> edition, Springer, USA (2003).

- [34] K Tanaka, T Shinji and H Uchiki, Photoluminescence from  $\text{Cu}_2\text{ZnSnS}_4$  thin films with different compositions fabricated by a sputtering-sulfurization method, *Sol. Energy Mater. Sol. Cells* **126** (2014) 143-148.
- [35] M Grossberg, P Salu, J Raudoja and J Krustok, Microphotoluminescence study of  $\text{Cu}_2\text{ZnSnS}_4$  polycrystals, *J. Photonics Energy* **3** (2013) 030599 (6 pages).
- [36] J Lee, NC Giles, D Rajavel and CJ Summers, Room-temperature band-edge photoluminescence from cadmium telluride, *Phys. Rev. B* **49** (1994) 1668-1676.
- [37] M Grossberg, J Krustok, J Raudoja and T Raadik, The role of structural properties on deep defect states in  $\text{Cu}_2\text{ZnSnS}_4$  studied by photoluminescence spectroscopy, *Appl. Phys. Lett.* **101** (2012) 102102 (4 pages).
- [38] S Chen, A Walsh, X-G Gong and S-H Wei, Classification of Lattice Defects in the Kesterite  $\text{Cu}_2\text{ZnSnS}_4$  and  $\text{Cu}_2\text{ZnSnSe}_4$  Earth-Abundant Solar Cell Absorbers, *Adv. Mater.* **25** (2013) 1522-1539.
- [39] D Huang and C Persson, Band gap change induced by defect complexes in  $\text{Cu}_2\text{ZnSnS}_4$ , *Thin Solid Films* **535** (2013) 265-269.
- [40] JJS Scragg, JK Larsen, M Kumar, C Persson, J Sendler, S Siebentritt and C Platzer-Björkman, Cu-Zn disorder and band gap fluctuations in  $\text{Cu}_2\text{ZnSn}(\text{S,Se})_4$ : Theoretical and experimental investigations, *Phys. Status Solidi B* **253** (2016) 247-254.
- [41] T Hoshina and H Kawai, Luminescence excitation spectra and their exciton structures of ZnS phosphors: Mn, (Cu, Al), (Ag, Al) and (Au, Al) dopes phosphors, *Japanese J. Appl. Phys.* **19** (1980) 267-277.
- [42] DC Joy, *Monte Carlo Modelling for Electron Microscopy and Microanalysis*, Oxford University Press, New York (1995).
- [43] MJ Romero, H Du, G Teeter, Y Yan and MM Al-Jassim, Comparative study of the luminescence and intrinsic point defects in the kesterite  $\text{Cu}_2\text{ZnSnS}_4$  and chalcopyrite  $\text{Cu}(\text{In,Ga})\text{Se}_2$  thin films used in photovoltaic applications, *Phys. Rev. B* **84** (2011) 165324 (5 pages).

## Figure Captions

**Figure 1:** Conduction and valence band edge diagram for a heavily doped, *p*-type semiconductor. The red dotted line is the acceptor energy level. Carrier mobility ( $\mu$ ) at the band edges and recombination pathways are also indicated. These include ‘BT’ (band to tail), ‘TT’ (tail to tail), ‘TI’ (tail to impurity), ‘BI’ (band to impurity) and ‘BB’ (band to band) recombination.

**Figure 2:** (a) External quantum efficiency (EQE) curves for the CZTS device. The EQE Tauc plot is shown in (b), while (c) is a plot of  $\log[\log(1/1-\text{EQE})]$  vs.  $(E_g - E)^2$ , where  $E_g$  is the band gap and  $E$  the photon energy.

**Figure 3:** (a) SEM backscattered electron image of the CZTS front surface. The small, dark precipitates are ZnS, more clearly seen in the figure inset. EDX maps for copper, zinc, tin and sulphur are shown in figures (b)-(e) respectively, while figure (f) is the room temperature panchromatic CL image. All images were acquired from approximately the same area (the circled region is intended as a common ‘point’ of reference). Figure (g) is a FIB cross-section secondary electron image of the specimen.

**Figure 4:** Cumulative distribution profiles for (a) Cu/(Zn+Sn) and (b) Zn/Sn atomic ratios measured from two separate regions. The composition was measured for 100 specimen points within each region using SEM-EDX. The figure legends indicate the maximum and minimum atomic ratio values for the particular region of interest.

**Figure 5:** (a) Micro-Raman map of the ZnS principal component obtained using a 325 nm laser. The high ‘intensity’ regions show Raman spectra characteristic of ZnS. (b) is a typical Raman spectrum for CZTS obtained using a 785 nm laser source. The spatial variation of position and width of the  $336\text{ cm}^{-1}$  peak are plotted in (c) and (d) respectively, along with a histogram showing the distribution of values. The equivalent figure for the  $Q' = I_{336}/(I_{366} + I_{373})$  intensity ratio is shown in (e). In all cases the map dimensions are  $20 \times 20\text{ }\mu\text{m}$ .

**Figure 6:** (a) Secondary electron image of CZTS front surface and (b) the panchromatic CL image. Image (a) has been rotated to have the same orientation as (b); a surface contaminant has been circled in both images to act as a fiducial marker. The CL spectrum summed over the entire area in (b) is shown in (c). The specimen temperature was 10 K.

**Figure 7:** Spectra for the (a) second, (b) third and (c) fourth principal components from the data set in Figure 6. The scree plot is shown in (d). The dotted line is the linear trend line fitted to principal component numbers above 20.

**Figure 8:** Component maps for the (a) second, (b) third and (c) fourth principal components from the data set in Figure 6. The brightest region in each image is circled. CL spectra extracted from these regions are shown in (d). The spectra are vertically displaced and their peak intensity normalised for visual clarity.

**Figure 9:** Schematic of multiple reflection within a CZTS layer of thickness  $t$ .  $E$  is the electric field amplitude of light emitted at angle  $\theta$ .  $r_1$  is the reflection coefficient at the CZTS-back contact interface, while  $(r_2, t_2)$  are the reflection and transmission coefficients at the CZTS-air interface.

**Figure 9:** (a) Secondary electron image and (b) panchromatic CL image of the front surface of CZTS. The former is rotated to have the same orientation as the latter, and a contaminant particle has been circled in both images to act as a fiducial marker. The second principal component spectrum is shown in (c), along with its component map in (d). An exemplar region of higher principal component weighting is shown circled in (d). The specimen temperature was 10 K.

Figures

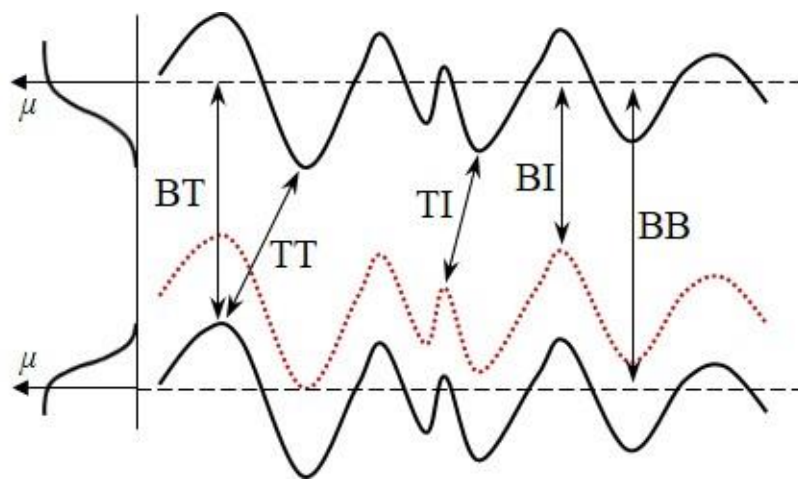
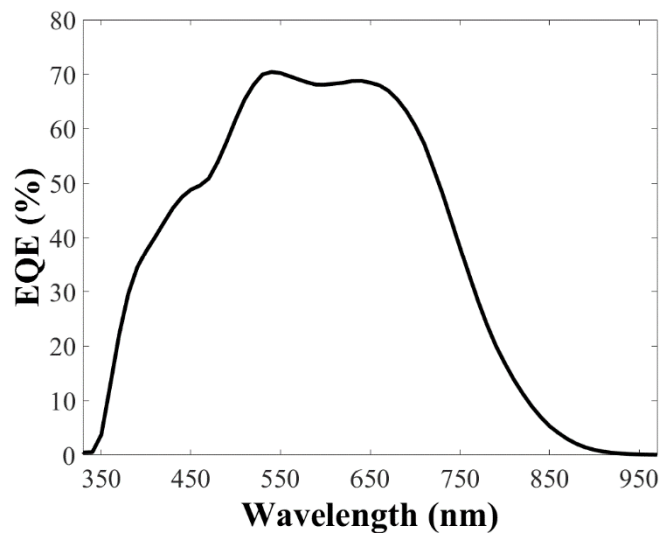
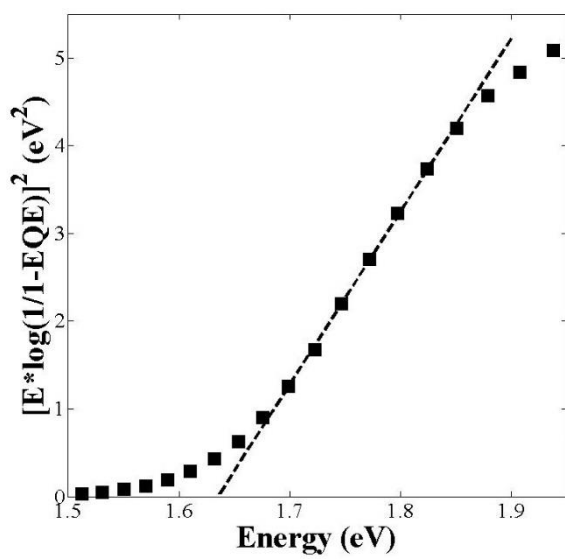


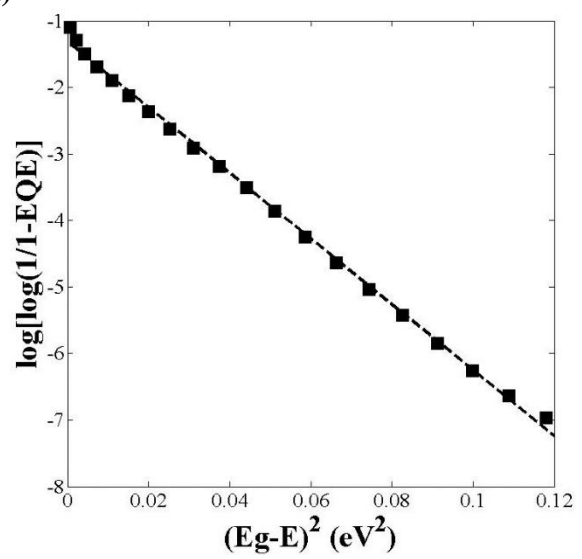
Figure 1



(a)

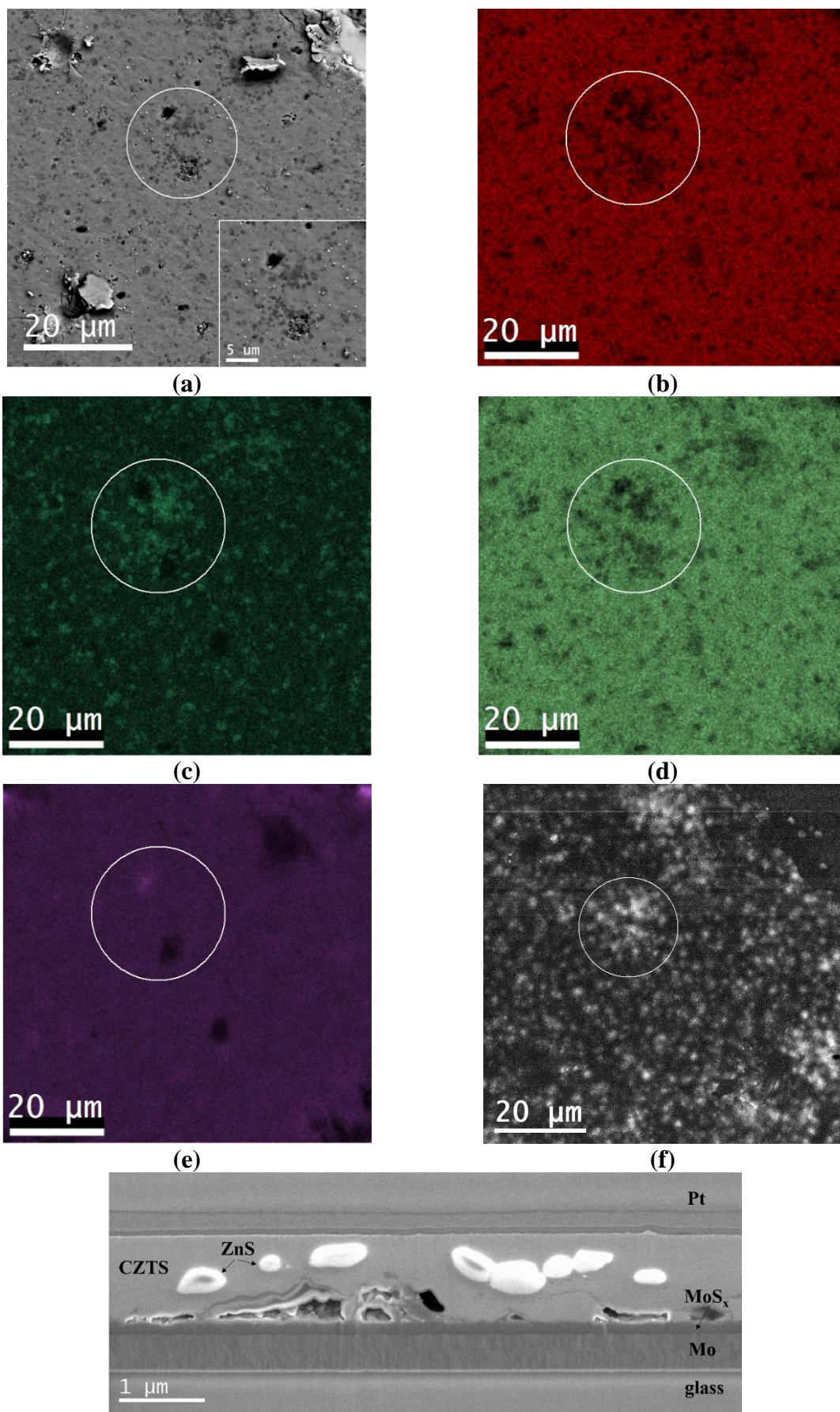


(b)

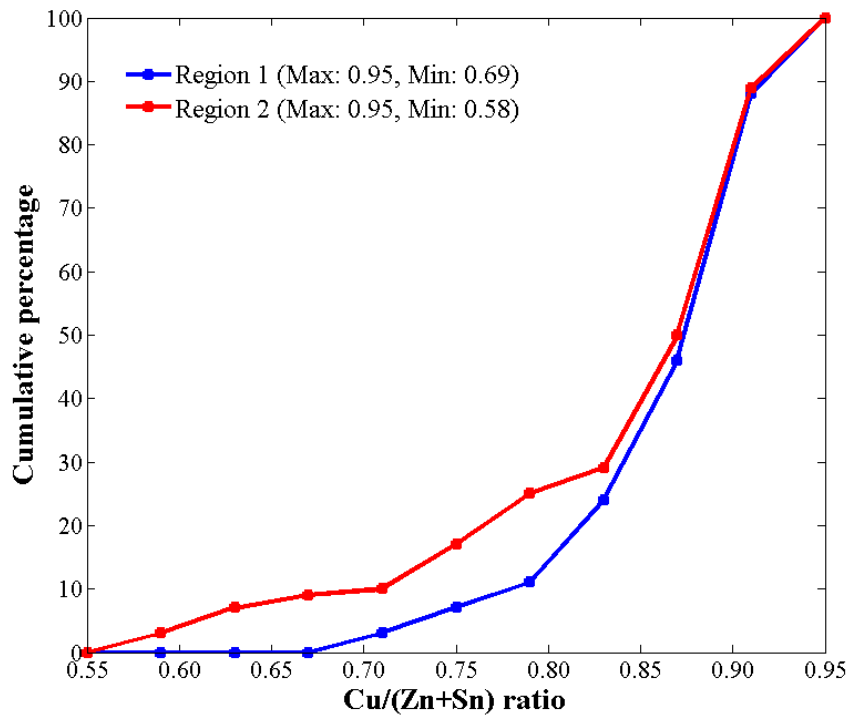


(c)

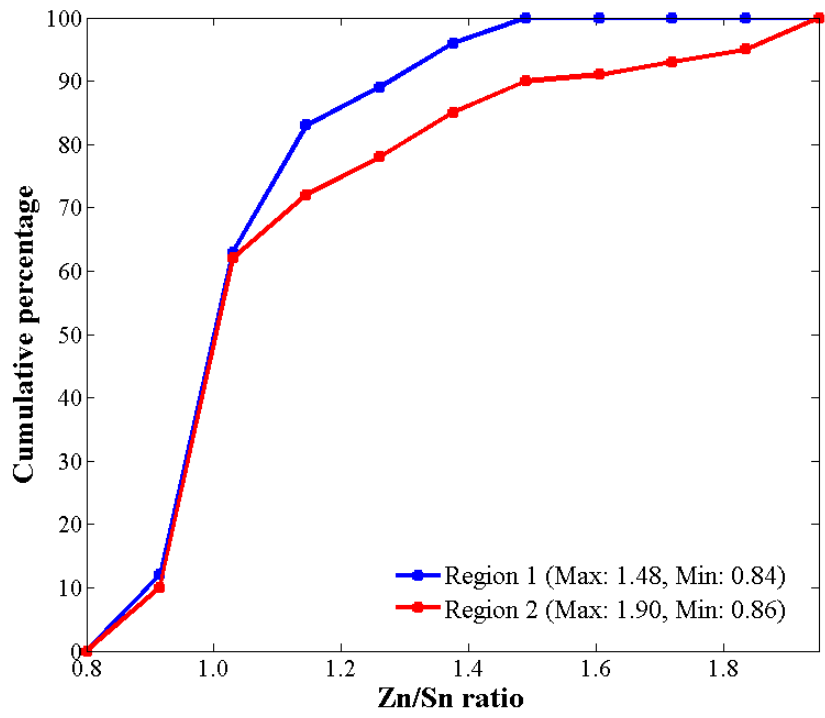
Figure 2



(g)  
Figure 3

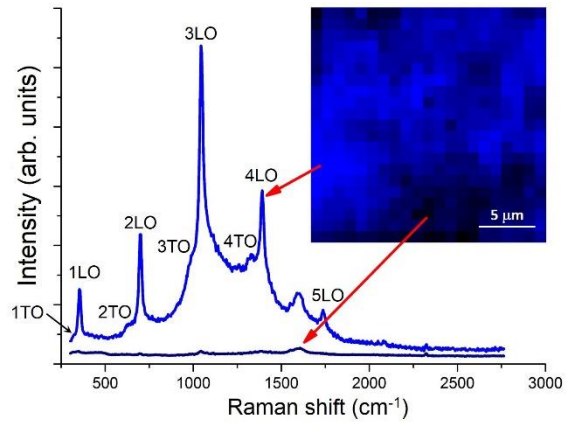


(a)

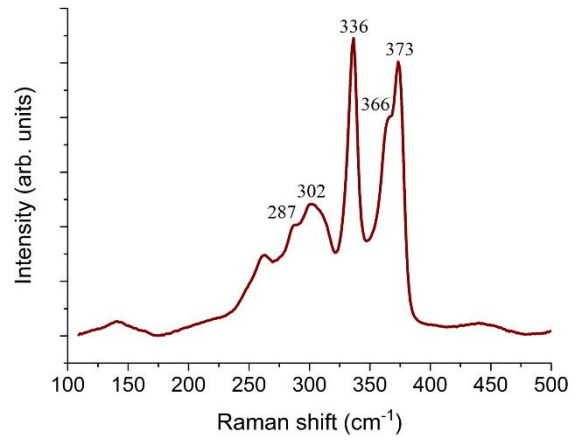


(b)

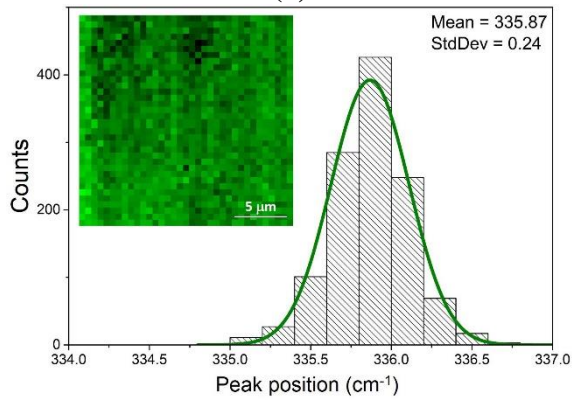
Figure 4



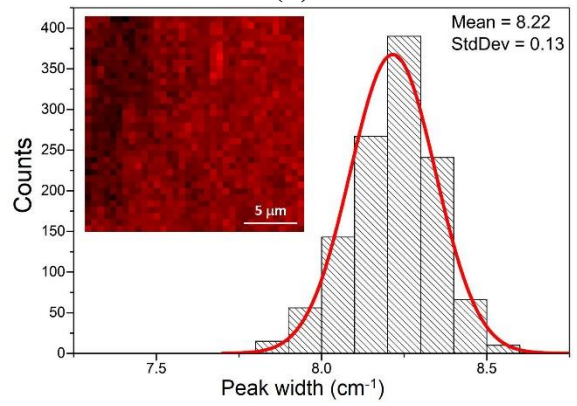
(a)



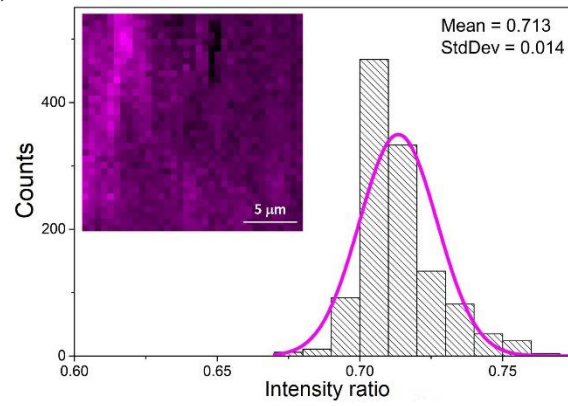
(b)



(c)

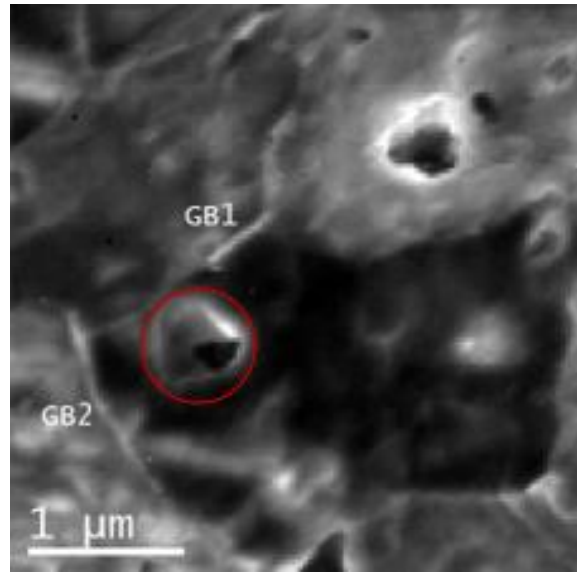
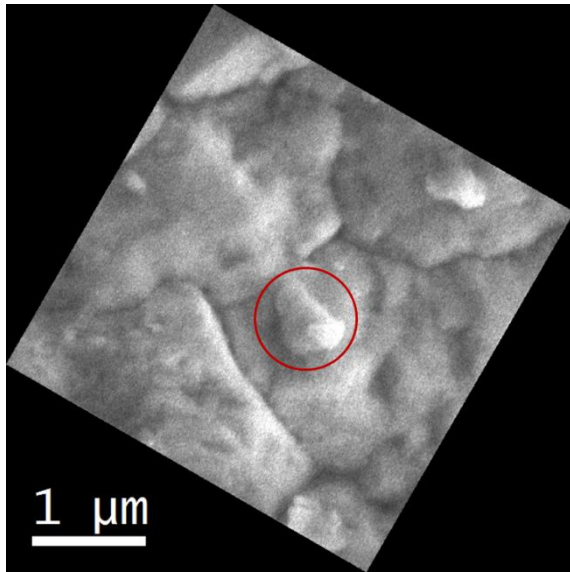


(d)



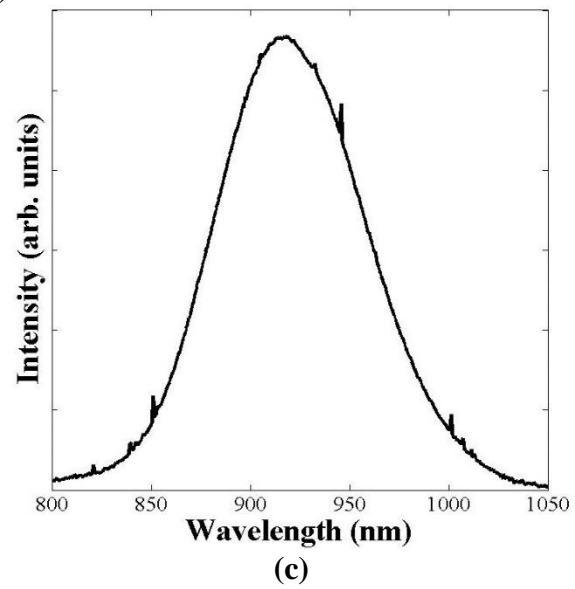
(e)

Figure 5

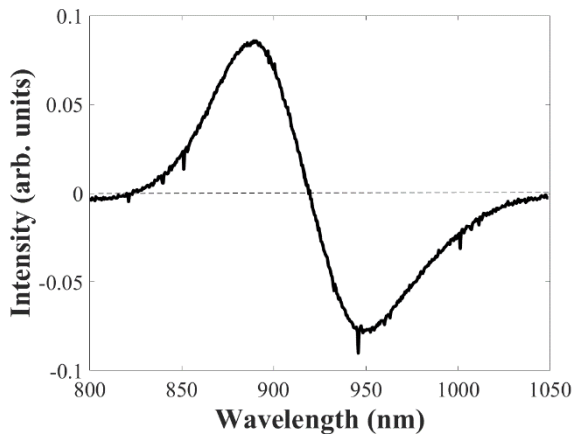


(a)

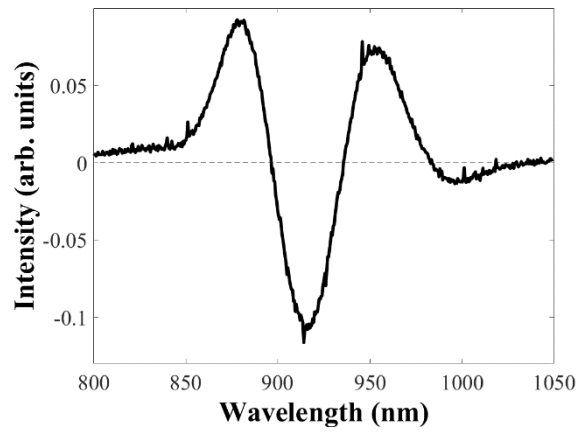
(b)



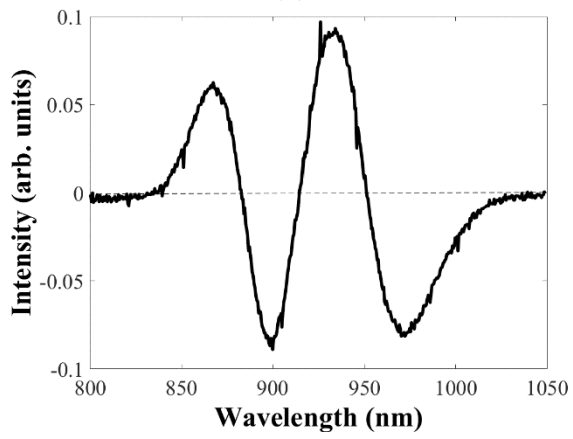
(c)  
Figure 6



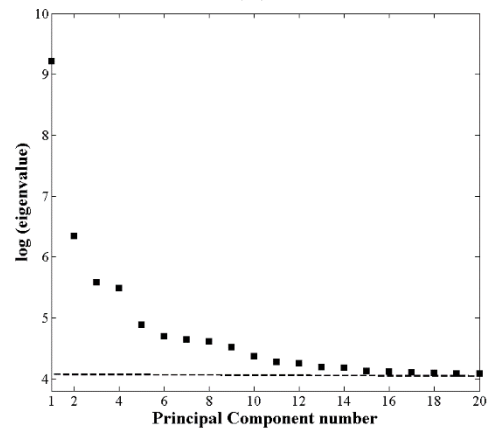
(a)



(b)



(c)



(d)

Figure 7

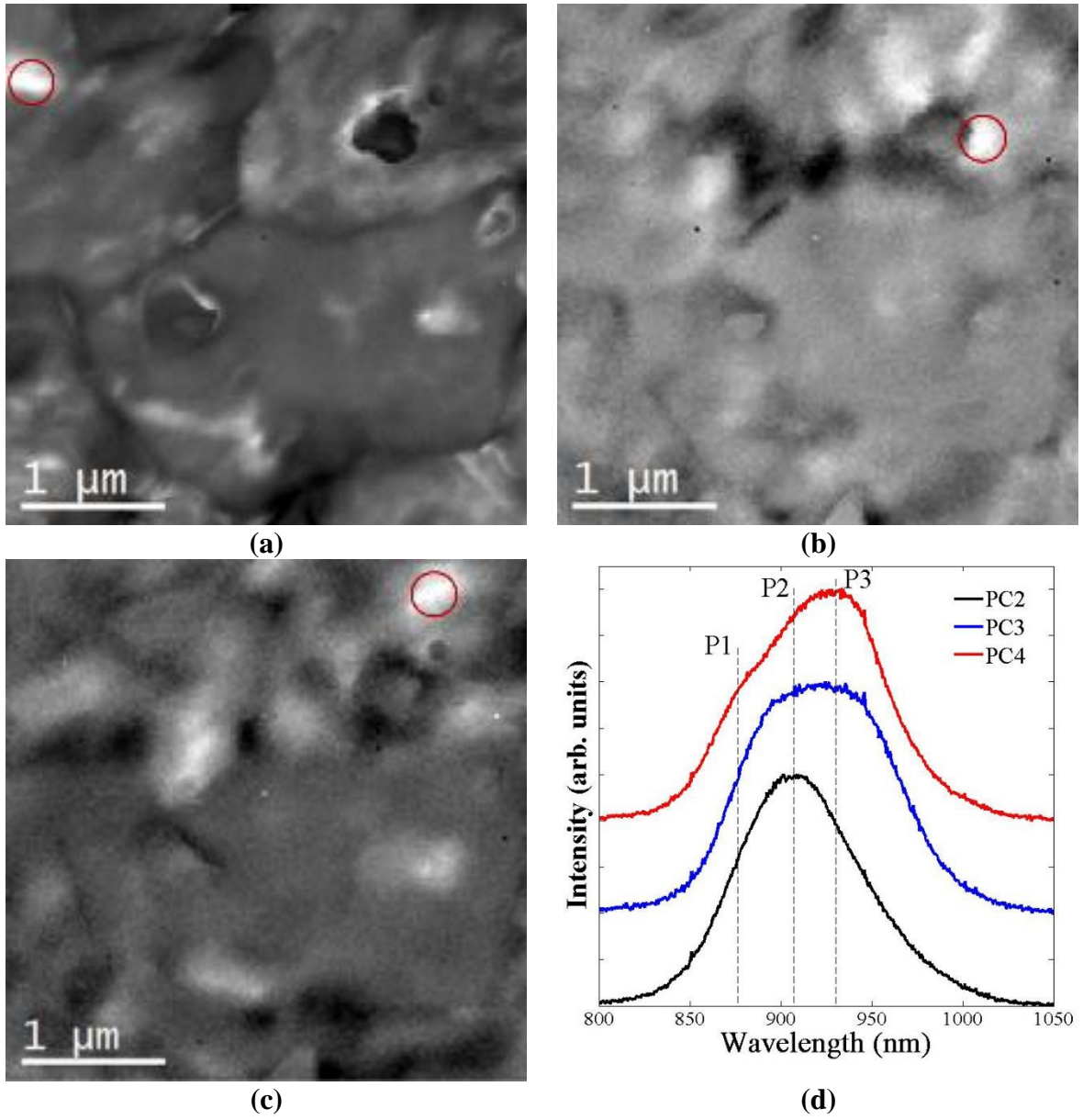


Figure 8

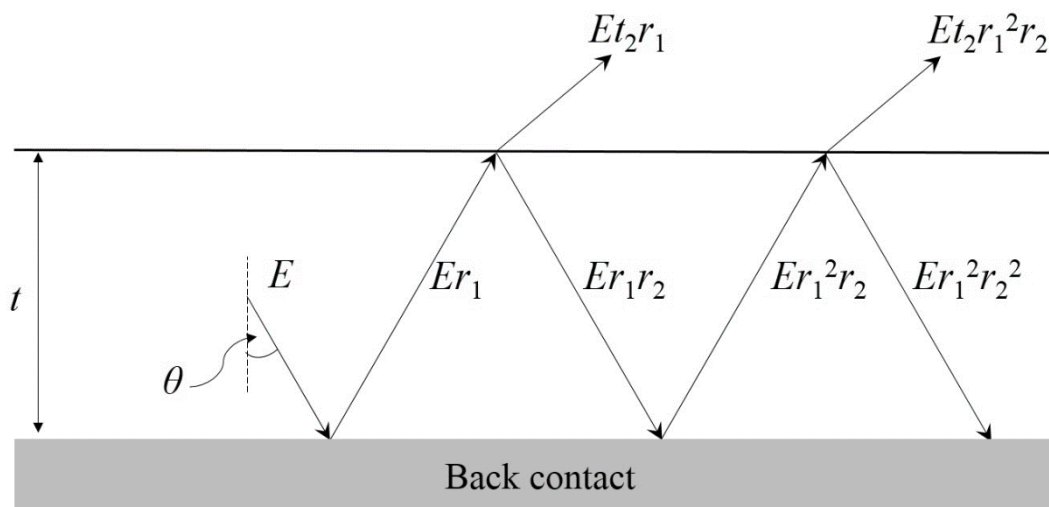
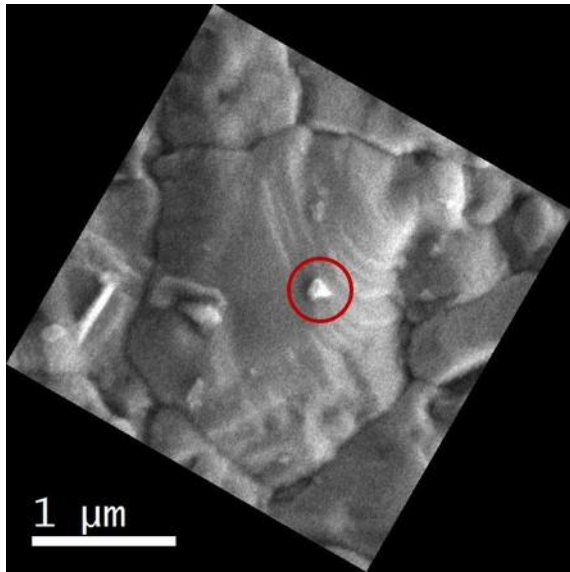
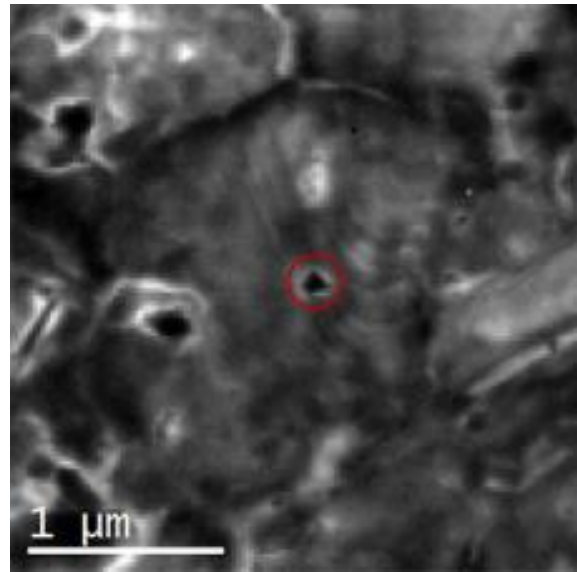


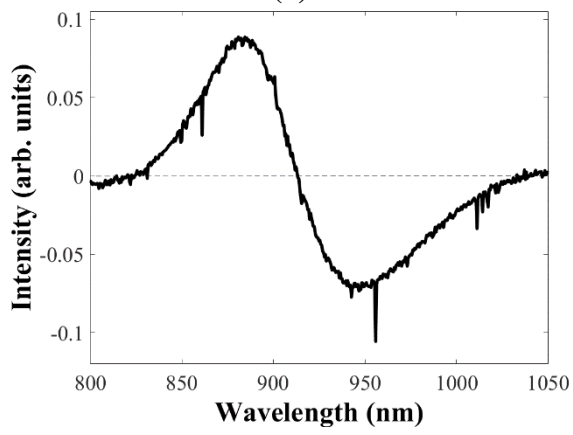
Figure 9



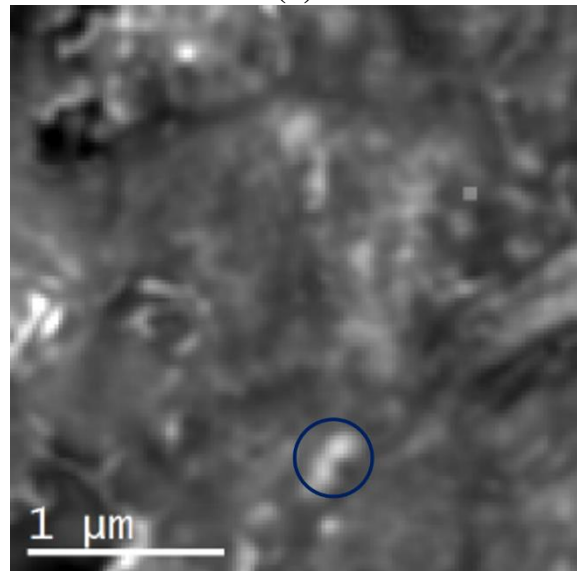
(a)



(b)



(c)



(d)

Figure 10